Materials Advances

ROYAL SOCIETY OF CHEMISTRY

PAPER

View Article Online
View Journal | View Issue

Cite this: *Mater. Adv.*, 2025, **6**, 4046

An outstanding, efficient visible-light-driven BiOI/$LaCoO_3$ Z-scheme system toward cefixime degradation†

Razieh Ahesteh,[a] Alireza Nezamzadeh-Ejhieh *[a] and Seyed Nezamoddin Mirsattari[b]

Multiple pollutants, especially antibiotics, are polluting water systems, prompting the development of novel photocatalysts with synergistic activity for mineralizing these pollutants. In this study, we synthesized three-dimensional BiOI microspheres, supported by noble metal-free $LaCoO_3$ co-catalysts, to construct an enhanced hybrid photocatalyst featuring superior charge separation properties. Various techniques were used to characterize the samples, including FTIR, SEM-EDX, XRD, and UV-Vis DRS (diffuse reflectance spectroscopy). Based on the Williamson–Hall equation, the BiOI/$LaCoO_3$ sample had an average crystallite size of 50.70 nm. BiOI, $LaCoO_3$, and BiOI/$LaCoO_3$ have band gaps of 1.80, 1.56, and 1.57 eV, relating to absorption edge wavelengths of 684, 790, and 789, respectively. For BiOI, $LaCoO_3$, and BiOI/$LaCoO_3$, the pHpzc (point of zero charge pH) values were 5.8, 10.5, and 8.9, respectively. In this coupled system, the moles of $LaCoO_3$ oxide are four times greater than those of another component, resulting in boosted activity. According to the response surface methodology (RSM) study, the suggested model shows a F-value of 50.26 > $F_{0.05,14,15}$ in the model, as well as a LOF F-value of 3.44 < $F_{0.05,10,5}$ and high R^2-values (R^2 = 0.9908, pred-R^2 = 0.9989, and adj-R^2 = 0.9996). The proposed binary catalyst of BiOI/$LaCoO_3$, the direct Z-scheme, is the preferred method of illustrating Cefixime photodegradation. Using chemical oxygen demand (COD) data, we could derive the rate constants of 0.053 min^{-1} and 0.061 min^{-1} for photodegrading solutions. During photodegradation, CEF molecules degrade at a $t_{1/2}$ of 13.07 and mineralize at a $t_{1/2}$ of 11.36.

Received 27th March 2025,
Accepted 25th April 2025

DOI: 10.1039/d5ma00279f

rsc.li/materials-advances

1. Introduction

Among the most important categories of pharmaceutical compounds are antibiotics, used in animal and plant breeding and human health care.[1–3] However, these compounds are increasingly overused and can be found in the environment, particularly in aquatic environments.[4] Among the most commonly used antibiotics is Cefixime (CEF). Following its FDA approval in 1980, it has become one of the most widely used antibiotics on the planet. CEF is an antibiotic classified as a cephalosporin of the third generation and is widely used. There are many antibiotics containing active pharmaceutical ingredients (API). These antibiotics are intended to treat various human and animal illnesses. Still, due to their extensive use and persistence in water sources, soils, and sediments, they have a negative environmental impact. Despite their non-biodegradability, many antibiotics make conventional chemical and biological treatments ineffective, resulting in increased levels of the original drugs and their intermediates on both land and water. Thus, methods for decomposing and removing antibiotic compounds from water sources (surface water, groundwater, or wastewater) are essential. AOPs (advanced oxidation processes, including photochemical, electrochemical, and catalytic oxidation, ozonation, Fenton and photo-Fenton, and Sonolysis) are among the various wastewater treatment methods that have attracted increasing attention to remove organic pollutants in wastewater.[5–7] Most of these methods employ *in situ* formation of highly reactive species (*e.g.*, hydroxyl radicals) that degrade and oxidize many organic pollutants and/or increase their biodegradability. The AOP systems still face several difficulties, such as inefficient energy use, reliance on specific materials, and/or introduction of additional chemicals.[8] In water and wastewater systems, heterogeneous photocatalysis is widely used to eliminate pharmaceutical and organic contaminants.[9–11]

This technique involves irradiating semiconductors with enough energy through photons (in the UV-Vis region).[12,13]

[a] *Department of Chemistry, Shah. C., Islamic Azad University, Shahreza, P.O. Box 311-86145, Islamic Republic of Iran. E-mail: r.ahesteh@iau.ir, arnezamzadeh@iau.ac.ir, arnezamzadeh@iaush.ac.ir, arnezam1346@gmail.com, Alireza_nezamzadeh@yahoo.com*

[b] *Department of Chemistry, Institute of Agriculture, Water, Food, and Nutraceuticals, Isf. C., Islamic Azad University, Isfahan, Islamic Republic of Iran. E-mail: n.mirsattari@iau.ac.ir*

† Electronic supplementary information (ESI) available. See DOI: https://doi.org/10.1039/d5ma00279f

With the photoinduced electron–hole (e^-/h^+) pairs, superoxide radicals and hydroxyl radicals are immediately produced in the presence of dissolved oxygen and water/hydroxyl.[14,15] In this process, these strong oxidants can break organic pollutants into smaller fragments, eventually breaking into H_2O and CO_2, and other inorganic ions depending on the structural heteroatoms.[16–18] The e^-/h^+ recombination, the critical heterogeneous photocatalysis' drawback, causes a significant reduction in overall process activity.[19–22] The number of techniques for decreasing e^-/h^+ recombination has increased over the past few decades. Semiconductor coupling creates a novel heterostructure to transport the photogenerated electrons from one semiconductor's negative CB to another's more positive CB.[23–28] There is an opposite trend between the holes between VB positions. Transitions of this kind reduce e^-/h^+ recombination while decreasing photodegradation.[26,29–33] In general, heterogeneous photocatalysis has a wide application range.[34–41]

BiOX is a VVI-VII ternary oxide semiconductor with an individual structure and a low band gap energy (E_g: 1.77–1.92 eV), capable of absorbing most visible light.[42,43] Although it has been regarded for sensitizing broadband semiconductors, it is highly recombinant in single semiconductors, resulting in poor activity since it cannot produce sufficient $^{\bullet}O_2^-$ and $^{\bullet}OH$, which are conducive to photocatalysis. Thus, many researchers have attempted to combine BiO-halides with other semiconductors to increase their separation efficiency.[44–47] It has been widely reported that bismuth oxide (BiOI) has a very narrow E_g of about 1.8 eV.[48,49]

It has been discovered that lanthanum cobaltite ($LaCoO_3$) is a highly efficient and reliable co-catalyst that is noble metal-free. $LaCoO_3$ is an essential member of the perovskite family of cobalt oxides, a vital semiconductor compound. Its excellent characteristics (excellent visible light absorption capacity and electronic conductivity, high charge carrier mobility, and low-cost, nontoxic compound) make it an excellent choice for CO_2 reduction and organic pollutant degradation.[42,44,50] The photocatalytic activity of a similar compound, $LaFeO_3$, has been well-reviewed.[51]

During the development of this study, nano-dimensioned BiOI and $LaCoO_3$ were synthesized, and their binary BiOI/$LaCoO_3$ catalyst was mechanically prepared. After confirming the synergistic effect of the binary system concerning the individual system in the photodegradation of cefixime (CEF), we investigated the impact of influencing variables on the degradation process by designing the experiment *via* an RSM approach. Finally, by performing the photodegradation tests against the scavengers (chloride, nitrate, ascorbic acid, and isopropanol act as scavengers of hydroxyl, electron, superoxide, and hole radicals, respectively), the relative roles of the reactive species in the overall photocatalytic activity were estimated.

2. Experimental

2.1. Materials and preparations

Cobalt nitrate hexahydrate (99.99%), lanthanum nitrate hexahydrate (99.99%), citric acid (99%), urea (99%), KI (AR), HNO_3 (AR), $Bi(NO_3)_3{\cdot}5H_2O$ (AR), and other chemicals were purchased from Sigma/Aldrich Co., Ltd, and used as received. All experiments were conducted with deionized water.

By modifying a published procedure, BiOI microspheres were produced by a facile solvothermal method.[52] An amount of 1.9400 g (4 mmol) $Bi(NO_3)_3{\cdot}5H_2O$ and 0.6640 g (4 mmol) KI is typically dissolved over 10 minutes in 40 mL ethylene glycol under critical stirring. The $Bi(NO_3)_3{\cdot}5H_2O$ solution was then added dropwise to the KI solution while vigorously stirring it. Vigorous stirring of the mixture was then performed for another hour at room temperature. A 100 mL Teflon-lined stainless-steel autoclave was used to heat the mixture at 160 °C for 12 hours after mixing. Centrifugation was used to collect the product after cooling naturally to room temperature, several washes with distilled water and ethanol, followed by 24 hours of drying at 80 °C.

Using a modified procedure, $LaCoO_3$ nanoparticles were prepared using sol–gel and citrate complexation. A 30 mL $La(NO_3)_3{\cdot}6H_2O$ solution (2.1650 g, 5 mmol) was added dropwise to a 30 mL aqueous solution containing 1.4552 g (5 mmol) of $Co(NO_3)_2{\cdot}6H_2O$ and 2.1014 g (10 mmol) of citric acid under stirring, and vigorous stirring continued at room temperature for 5 hours. The solution was then heated to 80 °C for 2 hours, and a xerogel-like precursor was formed. Then, it was dried in an oven at 100 °C for 12 hours. The precursor was powdered over the milling in an agate mortar, transferred to an aluminum crucible, and air calcined at 700 °C for four hours (rising temperature rate: 20 °C min^{-1}). After careful washing with water and ethanol, the black powder was dried at 80 °C for 12 h.[53]

To fabricate the binary system (BiOI/$LaCoO_3$), depending on the BiOI:$LaCoO_3$ molar ratio requested, the adequate weight of BiOI and $LaCoO_3$ NPs was added to an agate mortar and completely hand-mixed for 30 min.

Cefixime solution: a Cefixime tablet (400 mg) was weighed. To obtain an analytical sample, 3 cefixime tablets were completely turned into powder in an agate mortar, and 6.25 mg of the powder was completely dissolved in water and filtered in a 250 mL volumetric flask, reaching the mark to achieve a 100 mg L^{-1} stock CEF solution. This stock solution was used to prepare diluter solutions *via* the serial dilution pathway.

2.2. Characterization techniques

In this study, different analyses were conducted on the synthesized nanoparticles. Analyzing the samples' powder X-ray diffraction patterns (XRD) identified their crystal structure (PW1730, Philips Company, Netherlands). A Fourier Transform Infrared (FTIR) spectrophotometer (Agilent PerkinElmer Spectrum 65) was used to identify functional groups in the samples. Nanoparticle size and morphological and structural information were achieved with a field emission scanning electron microscope (FESEM), coated with gold (Tescan Company, Czech Republic). An elemental composition of photocatalysts was determined using energy-dispersive X-ray spectroscopy (EDX) (Quantum 200, USA). A UV-Vis diffuse reflection spectrum (DRS: Biomate5, Thermo Company USA) was used to obtain the optical features of catalysts. A UV-Vis spectrophotometer (PG-Instrument T80, Australia) was used to record absorption spectra

of cefixime solutions before and after the photodegradation process. The NPs were separated using a centrifuge instrument (Sigma).

2.3. Photodegradation tests

During the preliminary photodegradation tests of CEF, 3 mg of the alone and binary systems (BiOI or $LaCoO_3$ or BiOI/$LaCoO_3$) was added to 10 mL 10 mg L^{-1} CEF solution and homogenized in the dark for 10 min under magnetic stirring. Under this circumstance, an equilibrated surface adsorption/desorption was achieved, and the catalyst species were well-separated and dispersed. We irradiated the suspensions with three 40 W W-lamps for a specific time, centrifuged the suspension (at rpm ~13 000), and acquired the absorption spectrum of the supernatant (A). All experiments were done at room temperature. The reaction efficiency was compared with the absorbance of a blank CEF solution (A_0) to calculate the photocatalytic degradation efficiency. The formula was applied to calculate the CEF degradation percentage, in which C_0 is the initial CEF concentration and A is the CEF concentration at time t after photodegradation, according to Beer–Lamberts' law.

$$\text{CEF Deg. (\%)} = [(A_0 - A)/A_0] \times 100 = [(C_0 - C)/C_0] \times 100 \quad (1)$$

The effect of the direct photolysis in the absence of the catalysts and the effect of the surface adsorption on the CEF removal by the individual and binary catalysts (under the dark condition) were also studied under the same conditions mentioned above.

3. Results and discussion

3.1. Characterization studies

3.1.1. XRD analysis. Many of XRD's applications are to identify phases and characterize crystallographic structures.[54] Fig. 1 shows the X-ray diffraction patterns of BiOI, $LaCoO_3$, and $LaCoO_3$/BiOI hybrid materials. In agreement with the literature, all diffraction peaks are correctly assigned to tetragonal phase BiOI (JCPDS no. 73-2062). These reflect well-resolved (002), (102), (110), (112), (004), (104), (114), (212) and (115) reflections.[55] Observations on $LaCoO_3$ showed six characteristic diffraction peaks located at 23.23°, 32.88°, 33.30°, 40.65°, 47.50°, and 58.95°. The crystal planes (012), (110), (104), (202), (024), and (214) of the rhombohedral $LaCoO_3$ can be readily assigned according to the JCPDS Card No. 48-0123.[56,57]

A striking aspect of the findings was the similarity in XRD patterns between the obtained $LaCoO_3$/BiOI hybrids and pure BiOI. Furthermore, in the XRD patterns of the $LaCoO_3$/BiOI hybrid, a visible peak showing $LaCoO_3$ (2θ = 32.88°) content emerged as the content of $LaCoO_3$ increased, providing evidence that $LaCoO_3$/BiOI composites were successfully synthesized. Furthermore, no additional peaks associated with possible impurities were detected, indicating that the samples were of high purity as prepared. The average size of the sample crystallites was calculated using the Debye–Scherrer formula,

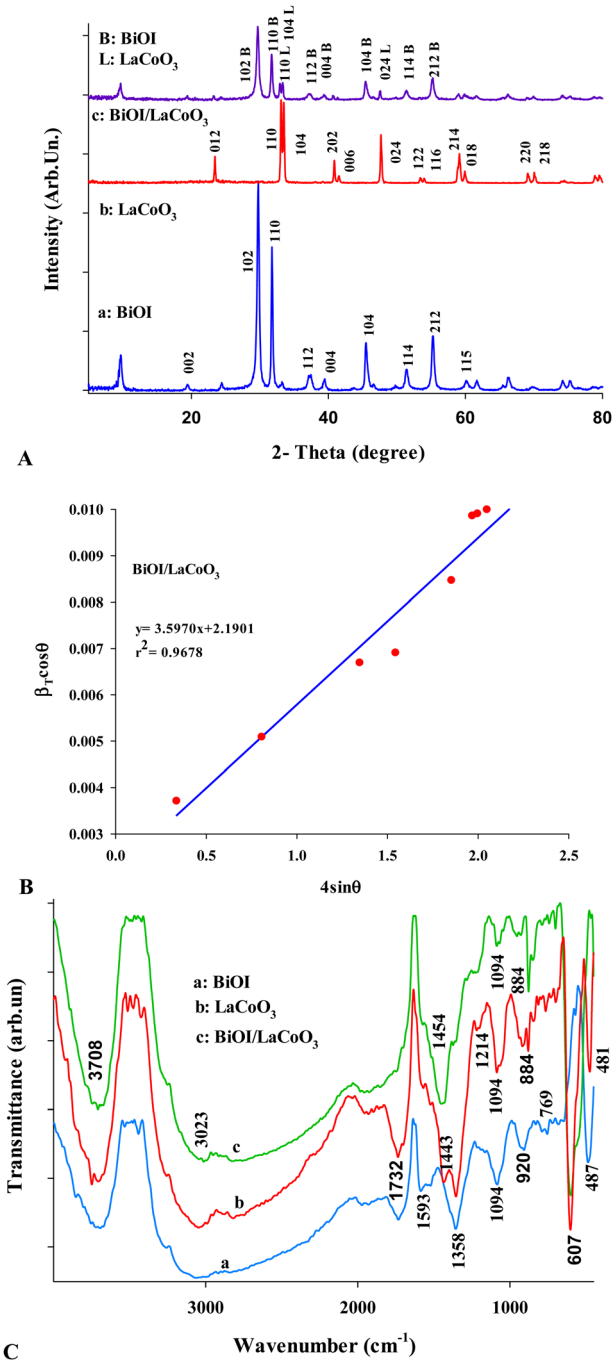

Fig. 1 XRD patterns (A), W–H plot (for the binary catalyst) (B), and FTIR spectra (B) of BiOI and $LaCoO_3$ NPs and the related binary BiOI/$LaCoO_3$ compound.

eqn (2),[58] and the Williamson–Hall (W–H) eqn (3).[59] The W–H model shows how the size (the Scherrer component) and the strain (ε, at ε = 0, W–H gives the Scherrer equation) simultaneously affect the peak broadening (D is the average size, D, β is the FWHM, the full width at half maximum, θ is the Bragg angle, k is the Scherrer constant (0.9), and λ is the X-ray source wavelength (Cu-Ka: 0.154 nm).[60]

$$D = (K\lambda)/(\beta \cos\theta) \quad (2)$$

$$\beta\cos(\theta) = (0.9\lambda/d) + (\varepsilon\sin(\theta)) \quad (3)$$

Averagely, the sizes of 23.06 nm, 31.87 nm, and 27.11 nm were respectively obtained for crystallites of BiOI, $LaCoO_3$, and the coupled photocatalyst, while the values for these crystallites were obtained by the W–H plot (see the ESI,† Fig. 1A and Fig. S1) were 195.41, 31.08, and 50.70 nm, respectively. A complete set of data, information, and results is also summarized in Tables S1–S3 (ESI†).

3.1.2. FT-IR spectra. The as-synthesized solid samples (BiOI, $LaCoO_3$, and BiOI/$LaCoO_3$) were analyzed and compared for their structural-functional groups by FT-IR. The Fourier transform infrared (FTIR) spectra of the resultant hybrid $LaCoO_3$/BiOI are illustrated in Fig. 1C as a further indication of the interaction between BiOI and $LaCoO_3$. $LaCoO_3$'s spectrum clearly shows that the prominent absorption peak at 601 cm^{-1} is attributed to the Co–O stretching mode.[61] Regarding pristine BiOI, the peak at roughly 523 cm^{-1} can be assigned to the Bi–O stretching mode.[62] Interestingly, with increasing $LaCoO_3$ content, the absorption peak of the Bi–O bond gradually shifted towards higher wavenumbers compared to the bare BiOI. This could be attributed to decreased electron concentration in $LaCoO_3$, as reported in the literature.[63]

3.1.3. UV-Vis-DRS and VB/CB potential positions. We have investigated the optical absorption features of BiOI and $LaCoO_3$ NPs alone and BiOI/$LaCoO_3$ binary systems using UV-Vis diffuse reflectance spectroscopy (DRS). Fig. 2A shows that the individual BiOI NPs exhibited a strong visible light response with an absorption edge wavelength (λ_{AE}) of 684 nm. For pristine $LaCoO_3$, a broad and strong light absorption was observed at wavelengths ranging from 200 to above 800 nm and the IR range. After attaching the $LaCoO_3$ co-catalyst onto the surface of BiOI, it was evident that the light absorption edges and absorption intensities of the BiOI/$LaCoO_3$ system was slightly redshifted. Co-catalysts containing $LaCoO_3$ can improve visible light utilization, but superfluous $LaCoO_3$ is detrimental to light absorption due to its shielding ability. In addition, $LaCoO_3$/BiOI hybrids exhibited strong, broad visible light absorption from 700 extended to the UV region with a λ_{AE} value of 787 nm, suggesting that the resultant hybrids would be an effective photocatalyst for purifying the environment in response to visible light, especially by using the solar spectrum as a cheap natural radiation source.

In addition, the band gap energy (E_g) of a typical semiconductor could be determined by a Kubelka–Munk equation[64–66] by using a typical Tauc formula of $\alpha h\nu = A(h\nu - E_g)^{n/2}$, where A, α, ν, and h are respectively the proportionality constant, absorption coefficient, frequency, and Planck constant. Typical semiconductor's optical transitions are indicated by n (n = 1 for direct transition, and n = 4 for indirect transition).[53,64,67] Various Tauc formula formats for different electronic transitions have been well illustrated and compared in the literature.[68]

Various Tauc formats have been used in the literature, all summarized in Table 1.[69] Another Tauc formula format is written as follows:

$$(\alpha h\nu)^n = k(h\nu - E_g) \quad (4)$$

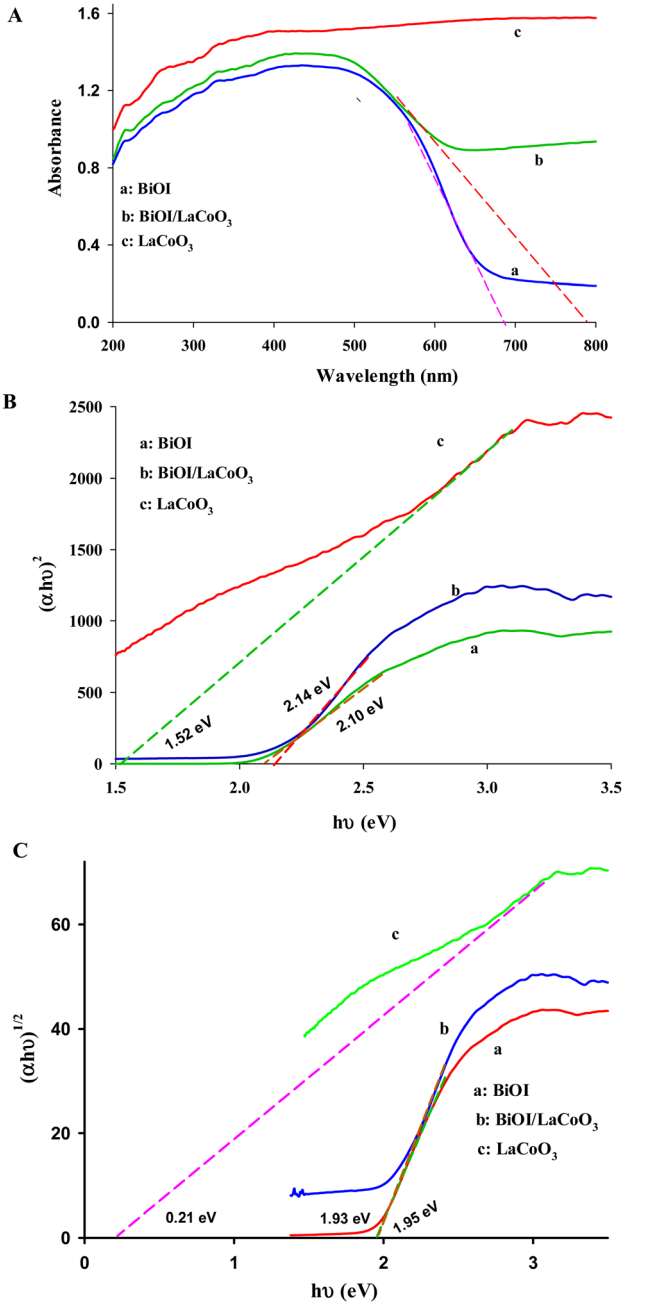

Fig. 2 (A) UV-Vis DRS absorption spectra of BiOI, $LaCoO_3$, and $LaCoO_3$/BiOI samples. (B) and (C) Tauc plots for E_g estimation for n = 2 and n = 1/12.

The exponent n is subjected to different values depending on the electronic transition type.[78–81] Typical Tauc plots for n = 2 and n = 1/2 can be seen in Fig. 2B and C (others are summarized in the ESI,† Fig. S2). Calculating E_g requires extrapolating the rising slope of curves toward the x-axis or photon energy. As a result of crossing the x-axis, the E_g is calculated for the definite electronic transition considered. A summary of all the values obtained is presented in Table 1.

The composite showed a considerable red shift concerning the bismuth oxycarbonate, indicating its ability to transfer electrons more efficiently. Using the following formulas (5)

Table 1 Optical and electrical features of the applied catalysts

Band gap energies

	Tauc plots (eV)				Absorption edge	
Catalysts	1/2	2	3/2	3	λ (nm)	E_g (eV)
BiOI	1.95	2.11	2.22	2.23	684	1.81
$LaCoO_3$	1.67	1.91	1.95	2.00	—	—
BiOI/$LaCoO_3$	1.90	2.00	2.05	2.10	789	1.57

The elemental electron affinity and ionization potentials

Element	E_a (eV)	E_i (eV)	$1/2(E_a + E_i)$ (eV)
Bi	0.94	7.24	4.09
I	3.04	10.45	6.75
La	−0.46	5.57	2.55
Co	−0.66	7.78	3.56
O	−1.46	13.62	6.08

Potential positions and Mulliken's electronegativities

Catalyst	χ (eV)	E_g (eV)	E_{VB} (eV)	E_{CB} (eV)
BiOI	5.92	2.11	+2.47	+0.36
$LaCoO_3$	4.62	1.91	+1.07	−0.84

Different formats of Tauc formula

	n-value for:				
Formula	IF	IA	DF	DA	Ref.
$F(R)\ h\nu = A(h\nu - E_g)^n$	3	2	3/2	1/2	70
$(F(R)\ h\nu)^n = A(h\nu - E_g)$	1/3	1/2	2/3	2	71
$(\alpha h\nu)^{1/n} = A(h\nu - E_g)$	3	2	3/2	1/3	72–74
$(\alpha h\nu) = A(h\nu - E_g)^{1/n}$	1/3	1/2	2/3	2	75,76
$(\alpha h\nu) = A(h\nu - E_g)^{n/2}$	6	4	3	1	77
$(\alpha h\nu)^{2/n} = A(h\nu - E_g)$	6	4	3	1	77

and (6) we calculated the valence (VB) and conduction band potentials (E_{VB} and E_{CB}) of BiOI and $LaCoO_3$ based on the E_g values for $n = 2$, the electron free energy (E_e; 4.5 eV *versus* SHE), and the electronegativity of semiconductors (χ).[82]

$$E_{VB} = \chi - E_e + 0.5E_g \quad (5)$$

$$E_{CB} = E_{VB} - E_g \quad (6)$$

The χ value is the geometric mean of the semiconductor's atoms' electronegativity. In addition, it is possible to calculate the atom's electronegativity from its first ionization and electron affinity (E_i and E_a), both of which can be calculated using the formula presented in Table 1.

3.1.4. SEM-EDX study analysis. SEM imaging (Fig. 3) of the surface nanostructures and surface morphologies of the BiOI, $LaCoO_3$, and the $LaCoO_3$/BiOI hybrid was performed using field-emission scanning electron microscopy (FESEM). An SEM image of pure BiOI, illustrated in Fig. 3A, shows pristine flower-like structures formed by numerous ultrathin nanosheets with a relatively smooth surface. In addition, the unique flower-like structure of BiOI nanosheets allowed exposure of sufficient anchor sites for LaCoO3 nanoparticles (NPs), enabling intimate contact with the NPs. $LaCoO_3$ exhibited a particle-like structure comprised of numerous irregular and agglomerated NPs, as shown in Fig. 3B. The SEM images taken at high magnification confirm that $LaCoO_3$ NPs adhered tightly

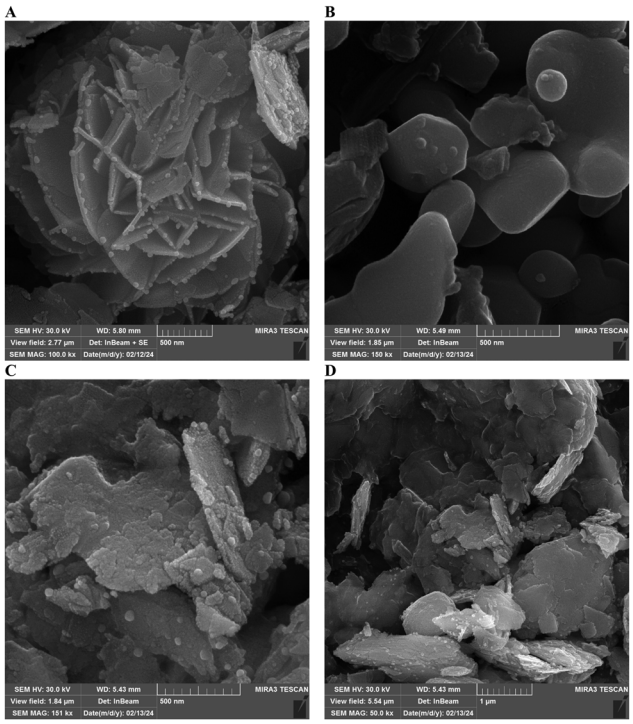

Fig. 3 SEM images of BiOI (A), $LaCoO_3$ (B) and $LaCoO_3$ (4.0 wt%)/BiOI hybrid (C) and (D).

to BiOI nanosheet surfaces with intimate contact, as shown in Fig. 3C and D. It is worth mentioning that the intimate contact in the binary system could be due to heterojunctions. The images show the dispersing of $LaCoO_3$ NPs onto the BiOI plate-like nanosheets.

Furthermore, energy dispersive X-ray spectrum analysis (EDS) and corresponding elemental mapping were performed to confirm the elemental composition and distribution in the hybrid $LaCoO_3$/BiOI. As confirmed by a homogeneous distribution of La, Co, O, Bi, and I elements in the hybrid, $LaCoO_3$ NPs were successfully immobilized on BiOI plate-like surfaces. It can be rationally inferred, based on the XRD, FTIR, SEM, EDS, and elemental mapping results described above, that the $LaCoO_3$/BiOI hybrid was not only well-fabricated but also that a uniform 0D/3D heterojunction exists between $LaCoO_3$ and BiOI that exhibits a strong interfacial interaction. There was a significant amount of contact area between $LaCoO_3$ NPs and BiOI nanosheets in this heterojunction, which increased the rate of interfacial charge transfer, ultimately allowing for increased photocatalytic activity.

3.1.5. The surface charge of the catalysts. We determined the pH_{pzc} of the prepared samples by fixing the pH (pH_I: initial pH) of 5 mL suspensions containing 0.01 g catalyst/0.01 M NaCl (as an adjuster for ionic strength) at values between 2 and 11. The final pH values (pH_F) were measured after 24 h stirring and applied for the drawing plots presented in Fig. 4. According to the first plot (Fig. 4A), pH_I–pH_I was used as the bisector. pH_{pzc} represents the pH value for each sample in which the environment solution has neutralized all the external charges, as determined by

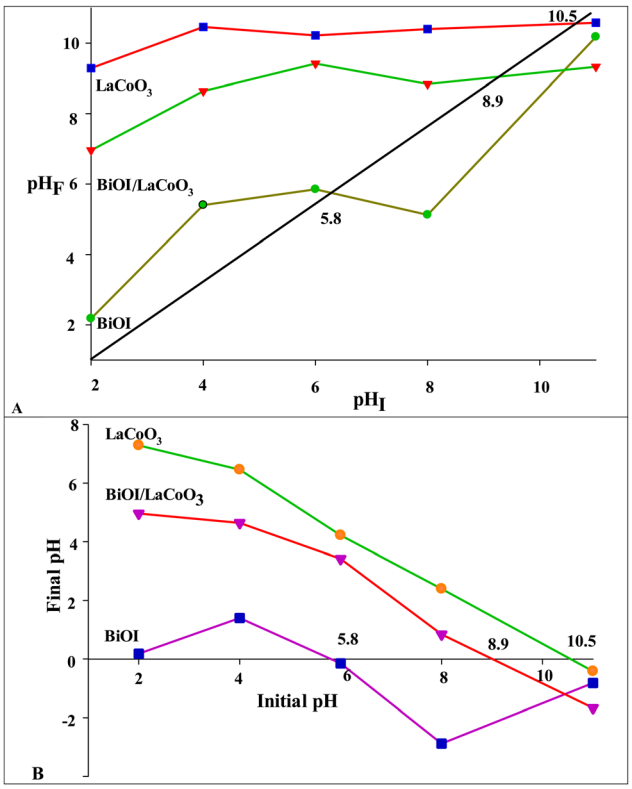

Fig. 4 Plots used to estimate the pHpzc of the samples.

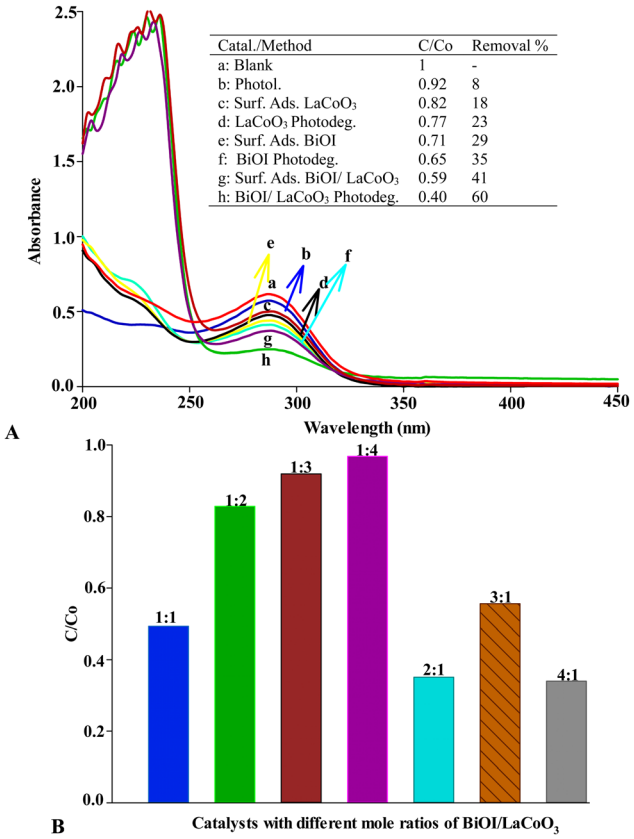

Fig. 5 (A) UV-Vis CEF absorption spectra over the applied removal processes (0.3 g L^{-1} of each catalyst in 10 mL of 10 mg L^{-1} CEF solution, time: 40 min, the mole ratio of BiOI : $LaCoO_3$ was 1 : 1); (B) the effect of the variation in the BiOI:$LaCoO_3$ molar ratio of the coupled catalyst on the CEF photodegradation.

the crossing point of pH_I–pH_F with the bisector. pH_{pzc} on the second plot (Fig. 4B) indicates the point where $pH_{initial}$ and pH_{final} are equal, so $\Delta pH = pH_{initial} - pH_{final} = 0$. In its native state before pH_{pzc}, the solid sample's surface (each catalyst investigated here) has an inherent negative (basic) feature capable of adsorbing protons of the aqueous solution, raising the solution pH and accumulating a net positive charge on the surface. The opposite is true, so when the solution pH exceeds the pHpzc, the surface positive (acidic) property causes the hydroxyl anions to adsorb from the aqueous solution, decreasing the solution pH and accumulating a net negative charge on the surface.[83,84]

3.2. Photodegradation experiments

3.2.1. Initial photodegradation experiments. The CEF UV-Vis absorption spectra in Fig. 5A show the decreased CEF maximum absorbance during different processes applied for its removal. The low removal efficiency of the direct photolysis (about 6%) reveals the high stability of CEF molecules over the illuminated photons. Comparing the photocatalytic degradation with the surface adsorption removal process proves the higher role of CEF photodegradation in each case. A boosted photocatalytic effect of the coupled catalyst concerning the single catalysts provides evidence for the higher e/h separation in this system (for better visibility of the compared absorption spectra, please see the ESI,† Fig. S3).

Fig. 5B shows the effects of the change in the components' moles in the coupled catalyst on the photocatalytic activity, and the highest activity was reached when the moles of BiOI were two times greater than that of another component. In this optimized value, the largest e/h pairs with the highest isolation extent were reached, which was used in the following steps (see Table S4, ESI†).

3.2.2. Designing experiments and analyzing the data. Based on the synergistic activity demonstrated above for the $LaCoO_3$/BiOI catalyst, we used the influencing factors, including pH (X_1), CEF concentration (X_2), catalyst dose (X_3), and illumination time (X_4) for designing the experiments by using an RSM approach and a central composite design (CCD). A summary of the selected ranges for these numerical factors can be found in Table 2. Corresponding 30 RSM run conditions are also summarized in Table S5 (ESI†). Randomization was used to minimize the impact of external variables on the response.[85] A response variable, y (the CEF photocatalytic degradation percentage), was determined for every run and used to obtain the following quadratic equation coefficients (using the DOE software version 11),[86] as shown by the second equation.

$$Y = \beta_0 + \sum \beta_i x_i + \sum \beta_{ii} x_i^2 + \sum \beta_{ij} X_i X_j + \varepsilon \quad (7)$$

$$Y = +78.28 - 3.64A + 7.01B - 10.06C + 1.98D - 0.5425AB + 2.45AC - 9.49AD + 6.39BC - 0.2800BD + 4.89CD - 1.08A^2 - 0.9167B^2 - 1.66C^2 - 1.61D^2 \quad (8)$$

Table 2 The influencing variables selected to design the experiments *via* the RSM approach and ANOVA results obtained in CEF photodegradation by the BiOI/$LaCoO_3$ catalyst

Chosen variables					
Code	Unite	$-\alpha$	-1 level	+1 level	$+\alpha$
A: pH	—	4	10	1	13
B: catal. dose	g L^{-1}	0.6	1	0.4	1.2
C: C_{CEF}	mg L^{-1}	6	16	1	21
D: time	min	30	80	5	105

ANOVA results					
Source	Sum squares	df	Mean sq.	*F* value	*p*-values
Model	6741.9	14	481.6	5026.3	<0.0001
A: pH	317.6	1	317.6	3314.5	<0.0001
B: catal. dose	1180	1	1180	12 315.5	0.0005
C:	2425	1	2425	25 326.5	<0.0001
D: time	95	1	95	987	<0.0001
AB	4.7	1	4.7	49.2	<0.0001
AC	96.2	1	96.2	1004.5	<0.0001
AD	1440	1	1440	15 028.2	<0.0001
BC	652.6	1	652.6	6811	<0.0001
BD	1.3	1	1.3	13.1	0.0025
CD	382	1	382	3989.2	<0.0001
A^2	32	1	32	331.9	<0.0001
B^2	23	1	23	240.6	<0.0001
C^2	76	1	76	790.5	0.0001
D^2	71.1	1	71.1	790.5	<0.0001
Residual	1.44	15	75.7		
Lack of fit	1.25	10	0.0958	3.44	0.0925
Pure error	0.1823	5	0.1255		
Cor total	6743.3	29			
Adj. R^2: 0.9989		Pred. R^2: 0.9996		R^2: 0.9998	

The results were statistically analyzed (ANOVA) at a 95% confidence level to validate the model's goodness. According to Table 2, the model is significant at a 95% confidence interval for the data processing compared to its *F*-value of 5026 with $F_{(0.05,14,15)} = 2.29$. To provide further evidence of the soundness of the model, we also analyze the non-significant lake of fit (LOF) term based on an *F*-value of $3.44 < F_{0.05,10,5} = 4.74$.[87]

The regression coefficient (R^2) value of 0.9998 confirms the model's total efficiency, indicating less than 1% of the total variations cannot be handled. There is a good degree of agreement in light of the close relationship between the experimental and predicted data. All variables selected significantly affected the response, as evidenced by the near value of R^2 and adjusted R^2 (0.9996). The predicted R^2 considers the model's ability to recognize new responses, which was achieved at a value close to the model's merit (0.9998) and predicted R^2 (0.9989). Furthermore, the closely predicted R^2 and the adjusted R^2 also agreed that additional variables had no effect on the response variable. A precision of greater than 4 (288.143) was also achieved, measuring the predicted response *versus* its standard deviation. The Pareto formula was used to predict the relative importance of each model's term. For the quadratic equation discussed above, β_i is the coefficient. A summary of the results is shown in Fig. S4 (ESI†).

$$P_i = \left(\beta_i^2 \Big/ \sum \beta_i^2\right) \times 100(i = 0) \quad (9)$$

3.2.3. Diagnostic and influencing plots. RSM recommended some diagnostic and influencing plots to evaluate the model's goodness. As a result of the plots, it became evident that the model is valid for experimental data processing. The plot in Fig. S4A (ESI†) illustrates the compliance of residuals from the normal distribution. A diagonal line should connect the data points if the model is correct. Otherwise, it is not correct. Accumulating all the data in one place should not have been possible. The graph should not have an S-shaped state, but converting the answer is a better way to provide a better analysis if this state is observed. Other diagnostic and influencing plots are collected in Fig. S4 (ESI†), all confirming the model's goodness.

3.2.4. 3D response surface plots. An illustration of the effect of time and catalyst amount on the degradation rate is shown in Fig. 6A. To achieve the highest degradation efficiency, a higher amount of photocatalyst must be irradiated for a longer time. In general, high concentrations of photocatalysts produce a significant scattering of incoming photons due to their negative effects. As a result of the accumulation of photocatalyst particles, the effective surface is reduced, and the destruction of cefixime is also reduced. Thus, a relatively smaller CEF degradation efficiency for 30 min can be compensated at longer illumination times.

A high catalytic amount, about 1 g L^{-1}, combined with pH 4 resulted in the greatest amount of degradation of cefixime in the study of the simultaneous effects of catalytic amount and pH on cefixime photodegradation (Fig. 6B). The binary catalyst has a pH_{pzc} about 8.9. At pH 4, its surface is expected to be positive. For CEF molecules, two carboxylic acid functional groups have pK_a values of 2.1 and 3.9, and most of the second carboxylic acid group will be in carboxylate form. Furthermore, its structure has two sulfur and five nitrogen heteroatoms and many oxygen atoms. Thus, the presence of anionic carboxylate and free electron pairs of these hetero atoms attract the CEF molecules by the catalyst's surface at pH 4, resulting in higher degradation efficiency. It would be expected that CEF anionic species at higher alkaline pHs critically repelled because of the repulsive force between both carboxylic functional groups (are in carboxylate anions) and high amounts of free electron pairs of the structural heteroatoms and the negatively charged catalyst surface. Thus, the lower degradation efficiency at pH 10 relatively compensated by increasing the catalyst dose that available more active sites for the degradation process.

Fig. 6C shows that the adverse effects of alkaline pH cannot be compensated at longer irradiation times. The results generally show lower CEF degradation at alkaline pH values, showing high stability of the anionic CEF because of the probable involvement of the free electrons in resonance effects. Higher CEF degradation efficiency at pH 4 and longer illumination times confirm the formation of relatively stable degradation intermediates that can be degraded at longer times.

Fig. 6D shows how pH and pollutant concentration affect the degradation, with a pH of about 4 and pollutant concentration of 6 mg L^{-1} giving the best degradation. At the mentioned pH, the catalyst is positively charged and protonated. Consequently, a repulsive force can cause degradation to decrease. These protonated

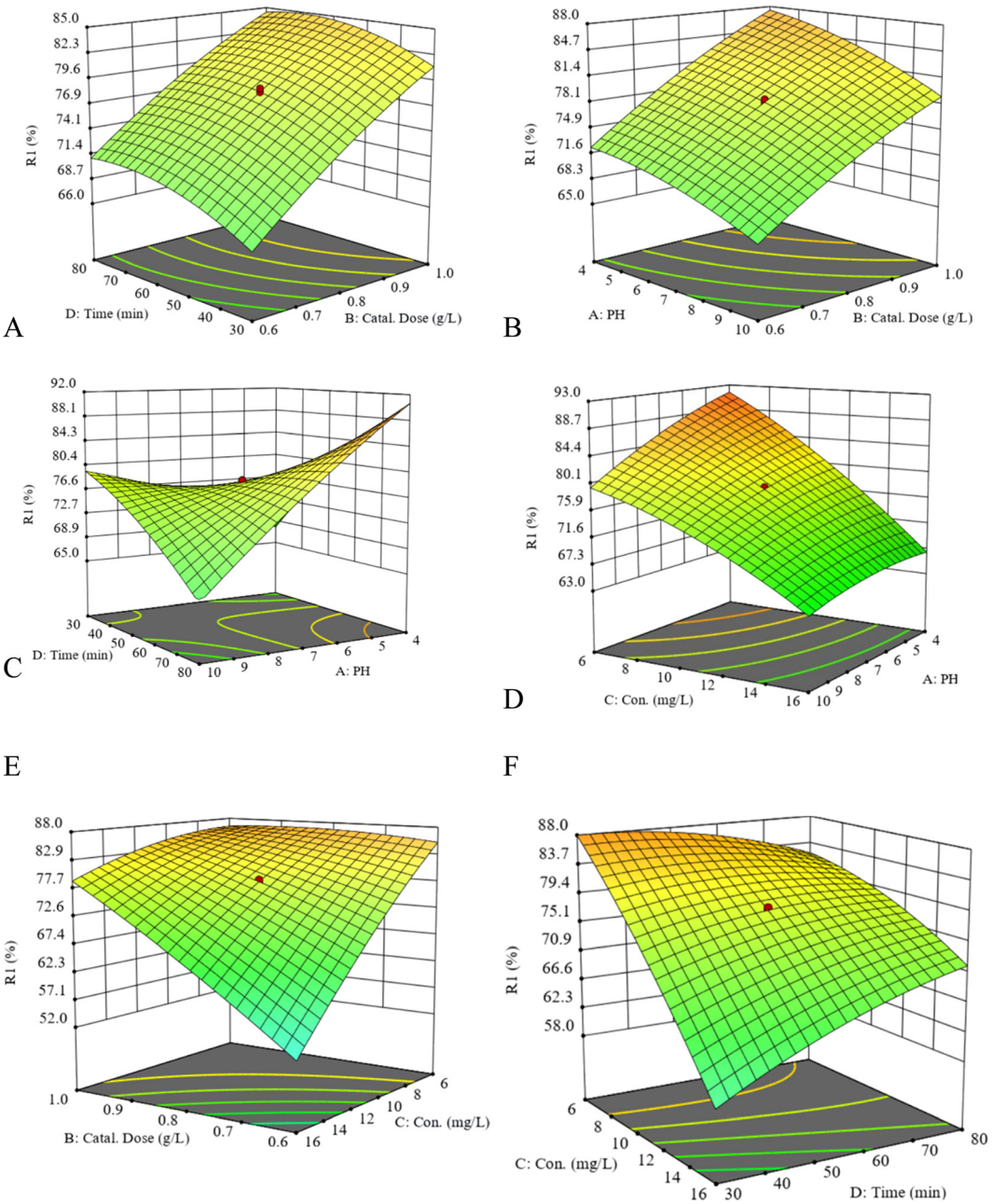

Fig. 6 3D response surface plot for CEF degradation by the coupled catalyst.

groups may, on the other hand, result in significant destabilization of the cefixime molecules, which allows for maximum degradation. In another way, in moderate concentrations, the collision probability between CEF molecules and the catalyst surface is high enough to reach the highest degradation efficiency. At higher CEF concentrations, H-bonding formation between CEF molecules may be high, resulting in lower interaction of CEF molecules with the catalyst surface. In the high CEF concentration, absorption of a significant part of the arrived photons by CEF molecules may result in the catalyst's lower photo-excitation and lower production of the reactive species.

According to the reasons mentioned above for the effects of the catalyst dose and CEF concentration, higher CEF efficiency can be reached at a lower CEF concentration of about 6 ppm and a higher catalyst dose of about 1 g L^{-1}, as shown in Fig. 6E. Finally, Fig. 6E shows the CEF molecules can be photodegraded at shorter times at a CEF concentration of 6 ppm. From the results, it can be concluded that some intermediate degradation radicles may react at longer times, forming larger species with harder degradation probabilities.

3.2.5. CEF photodegradation and photo mineralization kinetics. The next step was to do a kinetic study of CEF photodegradation. Eqn (10) shows that incident and transmitted intensities can be quantified using absorbed photons at specific wavelengths. Intensity symbols I_0 and I indicate incident and transmitted intensities, respectively. The Beer–Lambert law,

eqn (11), can be used to determine the *I*-value. C, b, and ε are the analyte concentration, cell diameter and molar absorption coefficient, calculated as follows.

$$A_\lambda = I_0 - I \quad (10)$$

$$I = I_0 \exp(-\varepsilon bC) \quad (11)$$

It has been proven by Grotthus–Draper's law that absorbed photons have a significant effect on photodegradation rates. Using eqn (12), you can calculate the rate of time-dependent photodegradation under constant irradiance (k_0 is a constant). By using a polychromatic beam, the equation above becomes eqn (13)

$$-\mathrm{d}C/\mathrm{d}t = k_0 \cdot I_0(1 - \exp(-bC)) \quad (12)$$

$$-\mathrm{d}C/\mathrm{d}t = k_0 \cdot I_0(1 - \exp(-bC)) \quad (13)$$

A solution based on eqn (14) can be used when photodegradation intermediates cannot absorb the arrived photons. Based on these formulas, we know that k_1 and ε_2 are the reactants' reaction rate constants and absorption coefficients, respectively.

$$\mathrm{d}C/\mathrm{d}t = k_1(1 - \exp(2C)) \quad (14)$$

Throughout the photodegradation process, photons are absorbed by degradation products, decreasing the number of photons absorbed. Thus, the solution absorbed a large amount of light related to the reactant. You can calculate degradation rates using eqn (15) (ε_3 is the degradation fragments' absorption coefficient).

$$-\mathrm{d}C/\mathrm{d}t = k_1[1 - \exp(-(2C + 3(C_0 - C)))](2C)/[(2C) + (C_0 - C)] \quad (15)$$

According to the formula below (k_1: the pseudo-rate constant), photodegradation can be predicted if the degradation fragments and reactants have similar absorption spectra (or $\varepsilon_2 = \varepsilon_3$).

$$-\mathrm{d}C/\mathrm{d}t = k_1[1 - \exp(-2C_0)][(C)/(C_0)] \quad (16)$$

A fourth type of photodegradation process involves high concentrations of reactants, in which the exponential term ($\exp(-(\varepsilon 2C + \varepsilon 3(C_0 - C))$) in eqn (16) reaches zero (*e.g.*, a zero-order rate process).

$$-\mathrm{d}C/\mathrm{d}t = K_1 \quad (17)$$

In terms of reaction kinetics, we can obtain a pseudo-first-order equation by using eqn (17) as an integral format of eqn (18). In consequence, this holds for most photocatalytic degradations including photon-absorbing reactants and intermediates.[88–94]

$$\ln(C/C_0) = -Kt (\text{or } C_t = C_0 e^{-kt}) \quad (18)$$

A series of photodegradation runs were done at various times to examine the kinetics of the CEF photodegradation using the $LaCoO_3$/BiOI catalyst.

Over time, the final CEF solution's absorbance was decreased, as shown in Fig. 7A. The C/C_0 value is calculated according to the maximum wavelength absorbance. Fig. 7B shows the results with the slope (0.053 min^{-1}) representing the CEF photodegradation rate constant as calculated using the Hinshelwood equation $Y = -0.0530X - 0.3590$ ($r^2 = 0.9743$). The $0.693/k$ equation can calculate the k-value for a $t_{1/2}$ time of 13.07 min. A photodegradation reaction takes about 13 min to degrade half of the CEF molecules under the applied conditions.

Chemical oxygen demand (COD) experiments were used to measure the mineralization values of CEF molecules during photocatalytic degradation. COD is the extent of the amount of oxygen needed to convert organic substances to inorganic substances, such as H_2O and CO_2. Other inorganic species can be formed by pollutant molecules depending on the nature of the heteroatom. This means that water or wastewater with a high COD content has a high pollution level. An extensive mineralization extent indicates that a more significant initial pollutant and its degradation fragments will be mineralized during photodegradation. One would expect a low COD value if a COD run was was carried out with such a solution. The results in Fig. 7D illustrate that parent CEF and its degradation fragments were mineralized, resulting in a lower oxygen consumption over the COD process.

As a result of the elongated photodegradation of CEF, the COD remaining in the solution decreased. Based on the COD data, Hinshelwood plots were created. A Hinshelwood equation is derived using Fig. 7C (inset), $Y = -0.0610X + 0.1660$ ($r^2 = 0.9957$) and a k-value of 0.061 min^{-1} ($t_{1/2} = 11.36$). During photodegradation, k-values were used to determine how fast the mineralized CEF molecules degraded. Based on the k-values, CEF photodegradation and CEF mineralization rates are comparable, and CEF degradation intermediates can be well mineralized during the photocatalytic process.

3.2.6. A study of the effects of scavenging agents. The degradative action of organic pollutants is achieved in a typical heterogeneous photocatalytic process by producing reactive species such as e^-, $^\bullet O^{2-}$, h^+, and $^\bullet OH$.[95] A study was conducted to determine the relative roles of the scavengers in the degradation rate of the proposed catalyst in the presence of $K_2S_2O_8$, $KHCO_3$, $C_2H_8N_2O_4$ and ascorbic acid (AA) (Fig. 8A). Photogenerated e^-, $^\bullet OH$, h^+, and $^\bullet O^{2-}$ can be trapped through the proposed trapping agents, respectively. As a result, their scavenging must reduce the overall photodegradation activity, demonstrating the critical role played by these reactive species in photodegradation.

In heterogeneous photocatalysis, peroxydisulfate (PDS), peromonosulfate, and hydrogen peroxide are electron scavengers. As a result of this scavenging process, PDS is produced as sulfate anion radicals ($SO_4^{\bullet -}$). There have been reported values of rate constants for PDS and sulfate radical reactions in the pH range of 3–8 involving acidic radicals.[96]

$$S_2O_8^{2-} + \text{heat} \rightarrow 2SO_4^{\bullet -} \quad (k_1\text{: } 5.7 \times 10^{-5}\ s^{-1})$$

$$SO_4^{\bullet -} + S_2O_8^{2-} \rightarrow S_2O_8^{\bullet -} + SO_4^{2-} \quad (k_2\text{: } 6.1 \times 10^{-5}\ M^{-1}\ s^{-1})$$

$$SO_4^{\bullet -} + H_2O \rightarrow {}^\bullet OH + H^+ + SO_4^{2-} \quad (k_3[H_2O] < 2 \times 10^{-3}\ M^{-1}\ s^{-1})$$

$$SO_4^{\bullet -} + SO_4^{\bullet -} \rightarrow S_2O_8^{2-} \quad (k_4\text{: } 5 \times 10^8\ M^{-1}\ s^{-1})$$

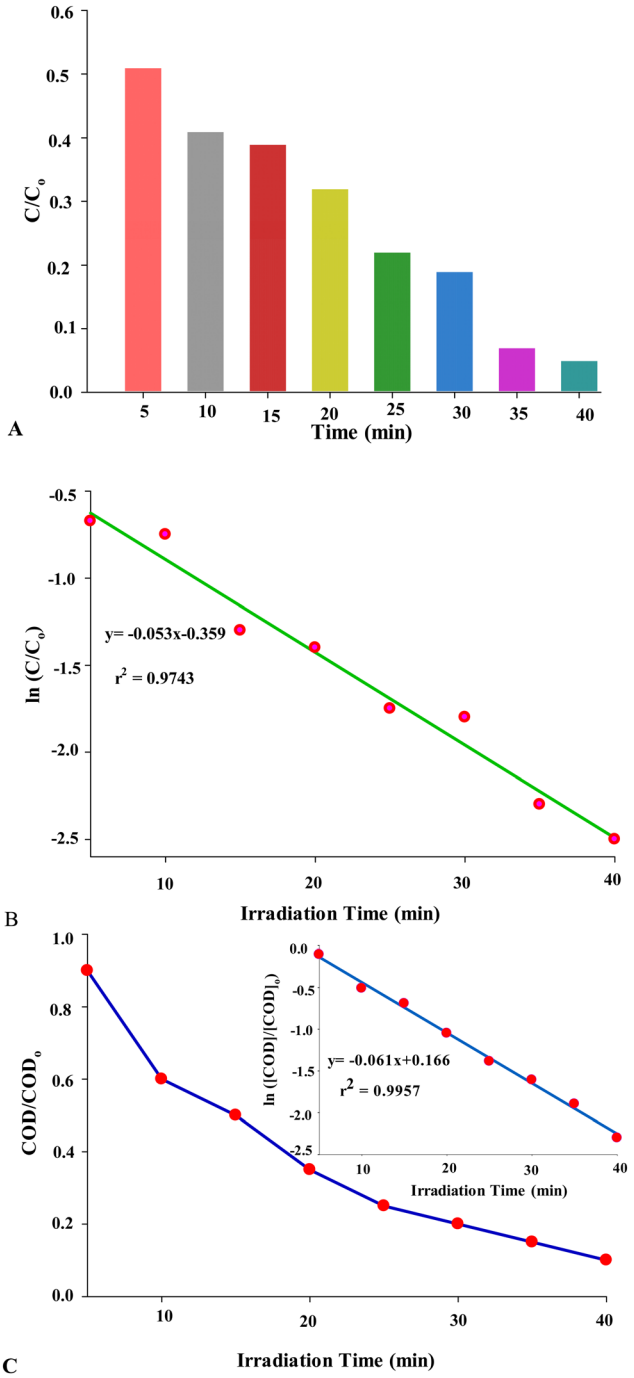

Fig. 7 (A) and (B) CEF photodegradation results *versus* time, and (C) COD results of the solutions obtained in case A (inset: the corresponding Hinshelwood plot).

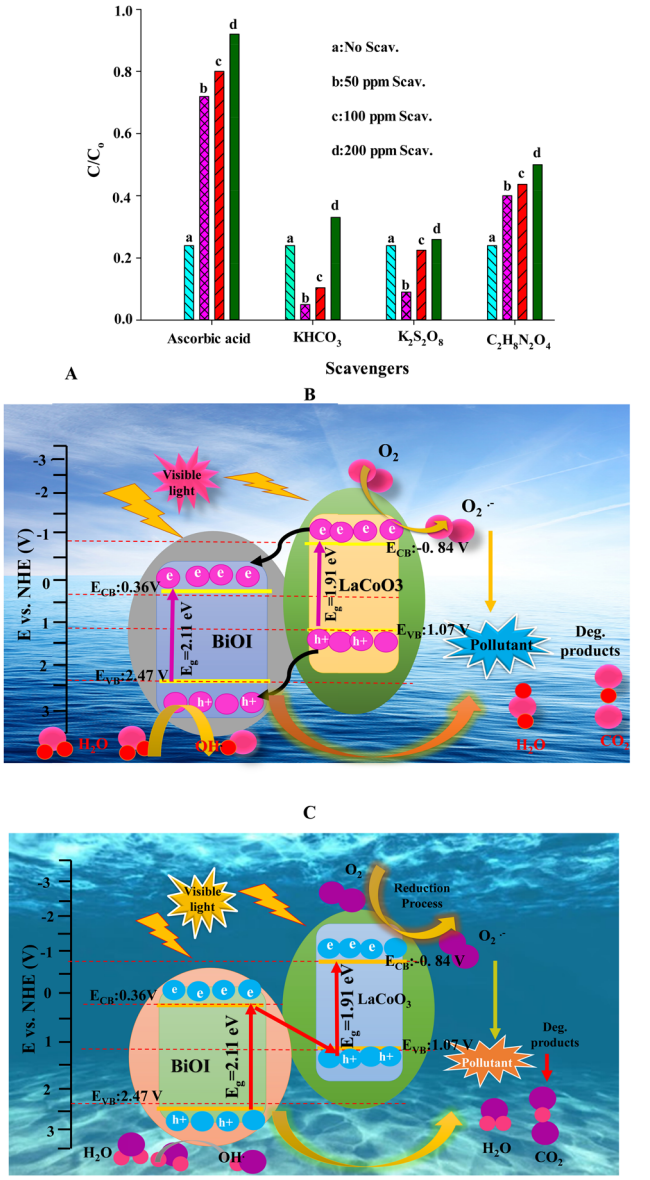

Fig. 8 (A) Results of scavenging agents in CEF photodegradation; (B) and (C) suggest mechanisms based on the results in case A.

It is possible to produce powerful •OH for photochemical decontamination of freshwater by exposing it to nitrates, nitrites, and dissolved organic matter (DOM).

Some solutes can also scavenge the radicals, including DOM itself, carbonate, and bicarbonate salts derived from inorganic carbon. Regarding kinetics, the scavenging reaction between •OH and carbonate or bicarbonate follows a second-order model (k: 3.9 × 10^8 M^{-1} s^{-1} and 8.5 × 10^6 M^{-1} s^{-1}, respectively). There is less reactivity in $CO_3^{\bullet -}$ produced compared to •OH.[97] As a hole scavenger, $C_2H_8N_2O_4$ has excellent performance.[98] Through the one or two electron steps redox reactions, ascorbic acid forms semi-dehydroascorbic acid and dehydroascorbic acid (DHA $+2H^+ + 2e^- \rightarrow$ ASC + H_2O, E° (pH 7) = 60 mV).[98]

Ascorbic acid can scavenge superoxide radicals. In the presence of acetaldehyde and xanthine oxidase (as the superoxide radical sources), scavenging of superoxide by AA has been reported to have a second-order rate constant of 8.2 × 10^7 M^{-1} s^{-1}. Scavenging reactions of this type have also been reported to have a rate constant of 2.7 × 10^5 M^{-1} s^{-1} (in the presence of the xanthine oxidase system).[99] Fig. 8A shows the inhibition trend as ascorbic acid > ammonium oxalate > $KHCO_3$ ≈ $K_2S_2O_8$, demonstrating the critical role played by

the photogenerated $^{\bullet}O_2^-$ followed by the $^{\bullet}OH$ in the photodegradation, based on the following trend.

Superoxide radicals > photogenerated h^+ > photogenerated e^- ~ hydroxyl radicals

This study shows that superoxide radicals and photoinduced holes play a relatively higher role in CEF photodegradation. The following section will discuss a photodegradation mechanism based on the results obtained here and the V_B/C_B positions obtained in the DRS section.

Several mechanisms have been described that illustrate photodegradation pathways (the charge carriers transfer) in heterogeneous photocatalysis up to this point. In addition, these mechanisms use direct Z-scheme photocatalysts,[100] traditional Z-scheme photocatalysts, S-scheme,[101–104] and Z-scheme types II heterojunctions, among others.[105,106] These mechanisms have been well-reviewed in the literature.[107–112] Usually, type-II photocatalytic mechanisms are used in heterojunction systems. When the semiconductors are considered to be successive binary heterojunctions, this mechanism is illustrated in Fig. 8B. In the fabricated binary catalyst, $LaCoO_3$ and BiOI also exhibit narrow band gaps, so they are appropriate for Vis light applications due to their ability to produce photo-induced e^-/h^+ pairs after illumination.

For the type-II heterojunction mechanism, photoinduced electrons must be transferred from the $LaCoO_3$-CB position (−0.84 V) to the BiOI-CB position (36 V). Alternatively, photoinduced holes should simultaneously migrate from BiOI-VB (2.47 V) to $LaCoO_3$-VB (1.07 V). Consequently, photo-induced electrons accumulate in the BiOI-CB position while the holes are in the $LaCoO_3$-VB position. The potential positions in this pathway show that the accumulated electrons in the BiOI-CB position, cannot reduce dissolved oxygen to superoxide species (E° = −0.28 V).

Fig. 8C shows a schematic depiction of the direct Z-Scheme mechanism. In this mechanism, BiOI-CB has a more negative potential (0.36 V) than $LaCoO_3$-VB (1.07 V). Thus, photoinduced electrons in BiOI-CB can be transferred to the $LaCoO_3$-VB position after being photoinduced. These electrons' photoexcitation finally results in e-accumulation in the $LaCoO_3$-CB position, as more potent than those accumulated in the BiOI-CB position (see the type II heterojunction mechanism). In other trends, hole-accumulation happened in the BiOI-VB position, as more potent than those accumulated in the $LaCoO_3$-VB (see the type II heterojunction mechanism). This description states that the photo-accumulated electrons in the $LaCoO_3$-CB position can only produce enough superoxide radicals (not by the photoinduced electrons in the BiOI-CB position). In another trend, the accumulated holes in the BiOI-VB position are strong enough to oxidize CEF molecules concerning the accumulated holes in the $LaCoO_3$-VB. Thus, the direct Z-scheme mechanism can describe the CEF photodegradation by the constructed binary catalyst.

3.2.7. Reusability of the catalyst. In order to accomplish repeatable runs, photodegradations were done in the optimal RSM run conditions (dose of BiOI/$LaCoO_3$: 1 g L^{-1}, pH 4, C_{CEF}: 6 ppm) at varied irradiation times. During photodegradation, the catalyst was separated, rinsed with water, dried at 80 °C for 10 min, and reused for the following photodegradation. Fig. 9A illustrates the results. In Fig. 9B, typical Hinshelwood plots are depicted based on the results. Linear plots displaying slopes are the rate constants of photodegradation, which were 0.0348, 0.0298, 0.0222, and 0.0158 min^{-1} for the first, second, third, and fourth reusing tests. It was confirmed that the proposed catalyst holds its activity under a relatively acidic pH of 4 over 4 reusing runs.

3.2.8. Comparison with other studies. As far as we know, compared with the photocatalytic research on various antibiotics and pharmaceutics, there are a few published papers on cefixime photodegradation. Some published papers in this regard are cefixime photodegradation by N-TiO_2/graphene oxide/titan grid sheets for visible light assisted photocatalytic ozonation,[113] cold atmospheric plasma/visible-light/N-TiO_2,[114] atmospheric air dielectric barrier discharge,[115] Fe_3O_4@GO nanocomposite,[116] and adsorption by activated sludge in the sequencing batch reactor.[117] It is worth mentioning that all of the techniques and catalysts used have their unique advantages. TiO_2 has UV band gaps, and it is hard to separate its particles, especially on a nano-scale, from the suspension at the end of the photodegradation process.

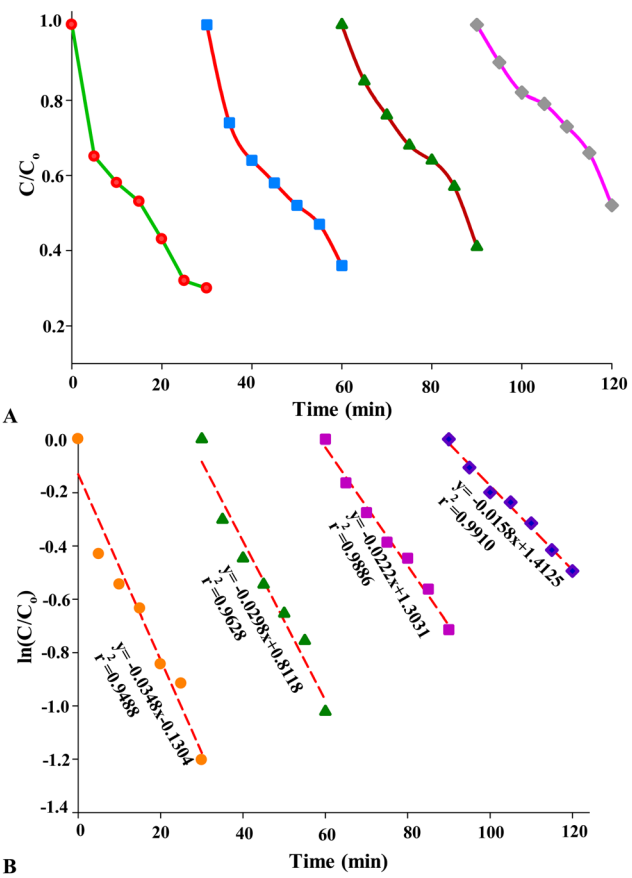

Fig. 9 Recycling runs of BiOI/$LaCoO_3$ for CEF photodegradation (dose: 1 g L^{-1}, pH 4, C_{CEF}: 6 ppm).

Fe-contained species activity depends on the pH, and if acidic pH is applied, it may dissolve and decompose catalysts. In the Fenton process, iron hydroxide precipitation decreases the activity and requires a second separation step to remove the precipitate. Some techniques need special techniques, as well as conditions and equipment. Here, the catalyst preparation is easy with catalytic activity under visible light.

Conclusions

This study reports the successful synthesis of a binary $LaCoO_3$/BiOI composite photocatalyst using a facile solvothermal approach. $LaCoO_3$ nanoparticles were immobilized onto the surface of flower-like BiOI species, resulting in a composite with better interface contact. As confirmed by the relative change in band gap energies of 2.32, 2.21, and 2.30 eV for BiOI, $LaCoO_3$, and BiOI/$LaCoO_3$ catalysts, the coupled catalyst experienced a small redshift relative to BiOI alone, but decreased the e/h recombination *via* the charge carrier transfer between two components. pH_{pzc} values of 5.8 and 10.5 were found for the BiOI and $LaCoO_3$ samples and 10.5 for the coupling sample, confirming the relative difference in native accumulated charges of the catalysts. The relative differences in average crystallite sizes obtained by the Scherrer and W–H formulas confirm the relative role of the strain effect in peak broadening. The $LaCoO_3$/BiOI composite exhibited significantly increased photocatalytic activity to degrade cefixime (CEF) under visible light illumination compared to single BiOI and $LaCoO_3$. A significant part of the improved activity can be attributed to the efficient charge transfer across the heterojunction interface created by the largely conductive $LaCoO_3$ co-catalyst as the acceptor of the photo-excited electrons in the CB-BiOI. Under visible light illumination, the reactive species scavenging runs indicated that superoxide radicals acted as the primary reactive agent for CEF degradation. Over time, the decreased COD impact of the photodegraded CEF solutions confirmed that the CEF degradation intermediates have relatively mineralized into water, carbon dioxide, *etc*.

Data availability

All data used and required are summarized in the ESI.†

Conflicts of interest

There are no conflicts to declare.

References

1 C. H.-F. Lau, K. van Engelen, S. Gordon, J. Renaud and E. Topp, Novel antibiotic resistance determinants from agricultural soil exposed to antibiotics widely used in human medicine and animal farming, *Appl. Environ. Microbiol.*, 2017, **83**, e00989–00917.

2 X. Dong, Y. Li, D. Li, D. Liao, T. Qin, O. Prakash, A. Kumar and J. Liu, A new 3D 8-connected Cd(II) MOF as a potent photocatalyst for oxytetracycline antibiotic degradation, *CrystEngComm*, 2022, **24**, 6933–6943.

3 M. Zheng, J. Chen, L. Zhang, Y. Cheng, C. Lu, Y. Liu, A. Singh, M. Trivedi, A. Kumar and J. Liu, Metal organic frameworks as efficient adsorbents for drugs from wastewater, *Mater. Today Commun.*, 2022, **31**, 103514.

4 B. Van den Bergh, J. E. Michiels, T. Wenseleers, E. M. Windels, P. V. Boer, D. Kestemont, L. De Meester, K. J. Verstrepen, N. Verstraeten and M. Fauvart, Frequency of antibiotic application drives rapid evolutionary adaptation of Escherichia coli persistence, *Nat. Microbiol.*, 2016, **1**, 1–7.

5 D. B. Miklos, C. Remy, M. Jekel, K. G. Linden, J. E. Drewes and U. Hübner, Evaluation of advanced oxidation processes for water and wastewater treatment–A critical review, *Water Res.*, 2018, **139**, 118–131.

6 J. Wang and S. Wang, Reactive species in advanced oxidation processes: Formation, identification and reaction mechanism, *Chem. Eng. J.*, 2020, **401**, 126158.

7 M. Liu, Y. Ye, J. Ye, T. Gao, D. Wang, G. Chen and Z. Song, Recent Advances of Magnetite (Fe3O4)-Based Magnetic Materials in Catalytic Applications, *Magnetochemistry*, 2023, **9**, 100.

8 M. A. Oturan and J.-J. Aaron, Advanced oxidation processes in water/wastewater treatment: principles and applications. A review, *Crit. Rev. Environ. Sci. Technol.*, 2014, **44**, 2577–2641.

9 M. Cai, Y. Liu, K. Dong, X. Chen and S. Li, Floatable S-scheme Bi2WO6/C3N4/carbon fiber cloth composite photocatalyst for efficient water decontamination, *Chin. J. Catal.*, 2023, **52**, 239–251.

10 D. Behera, P. Priyadarshini and K. Parida, ZIF-8 metal–organic frameworks and their hybrid materials: emerging photocatalysts for energy and environmental applications, *Dalton Trans.*, 2025, **54**, 2681–2708.

11 M. Liu, C. Shan, H. Chang, Z. Zhang, R. Huang, D. W. Lee, W. Qi, Z. He and R. Su, Nano-engineered natural sponge as a recyclable and deformable reactor for ultrafast conversion of pollutants from water, *Chem. Eng. Sci.*, 2022, **247**, 117049.

12 Y. Wu, X. He, X. Wang, J. Xv, M. Muddassir, I. A. Ansari and A. Zhong, Synergistic efficacy unleashed: Co/Ni-based catalysts as a versatile powerhouse for photocatalytic degradation of ornidazole, *Inorg. Chim. Acta*, 2024, **568**, 122115.

13 J. Wang, C. Rao, L. Lu, S. Zhang, M. Muddassir and J. Liu, Efficient photocatalytic degradation of methyl violet using two new 3D MOFs directed by different carboxylate spacers, *CrystEngComm*, 2021, **23**, 741–747.

14 P. Priyadarshini, A. Mishra, S. Nayak and K. Parida, NH2-MIL-125(Ti) and its functional nanomaterials – a versatile platform in the photocatalytic arena, *Nanoscale*, 2025, **17**, 4906–4957.

15 S. Subudhi, S. P. Tripathy and K. Parida, Metal oxide integrated metal organic frameworks (MO@MOF): rational

design, fabrication strategy, characterization and emerging photocatalytic applications, *Inorg. Chem. Front.*, 2021, **8**, 1619–1636.

16 A. Buthiyappan, A. R. Abdul Aziz and W. M. A. Wan Daud, Recent advances and prospects of catalytic advanced oxidation process in treating textile effluents, *Rev. Chem. Eng.*, 2016, **32**, 1–47.

17 M. Ahmaruzzaman, Biochar based nanocomposites for photocatalytic degradation of emerging organic pollutants from water and wastewater, *Mater. Res. Bull.*, 2021, **140**, 111262.

18 K. A. Isai and V. S. Shrivatava, Photocatalytic degradation of methyl orange using ZnO and Fe doped ZnO: A comparative study, *Iran. J. Catal.*, 2024, **9**(3), 259–268.

19 A. Rahmani-Aliabadi and A. Nezamzadeh-Ejhieh, A visible light FeS/Fe2S3/zeolite photocatalyst towards photodegradation of ciprofloxacin, *J. Photochem. Photobiol., A*, 2018, **357**, 1–10.

20 C. Shen, X. Li, B. Xue, D. Feng, Y. Liu, F. Yang, M. Zhang and S. Li, Surface plasmon effect combined with S-scheme charge migration in flower-like Ag/Ag6Si2O7/Bi12O17Cl2 enables efficient photocatalytic antibiotic degradation, *Appl. Surf. Sci.*, 2025, **679**, 161303.

21 A. Singh, A. K. Singh, J. Liu and A. Kumar, Syntheses, design strategies, and photocatalytic charge dynamics of metal–organic frameworks (MOFs): a catalyzed photodegradation approach towards organic dyes, *Catal. Sci. Technol.*, 2021, **11**, 3946–3989.

22 C. El Bekkali, H. Bouyarmane, S. Laasri, A. Laghzizil and A. Saoiabi, Effects of metal oxide catalysts on the photodegradation of antibiotics effluent, *Iran. J. Catal.*, 2024, **8**(4), 241–247.

23 C. Rao, L. Zhou, Y. Pan, C. Lu, X. Qin, H. Sakiyama, M. Muddassir and J. Liu, The extra-large calixarene-based MOFs-derived hierarchical composites for photocatalysis of dye: Facile syntheses and contribution of carbon species, *J. Alloys Compd.*, 2022, **897**, 163178.

24 R.-Q. Yan, G.-H. Liu, Q.-F. Wang, W. Liu and C.-L. Song, Fast Photodegradation of Malachite Green using Nano-ZnO on Ceramic MgAl Carbonate Layered Double Hydroxides Support, *Chin. J. Chem. Phys.*, 2016, **29**, 241–244.

25 M. Liu, G. Chen, Z. Song, Z. He, A. Zhong and M. Cui, Catalytic Dechlorination of Three Organochlorides by Recyclable Nano-Palladium-Engineered Natural Sponge with Formic Acid, *Catalysts*, 2024, **14**(7), 424.

26 J. Zhao, Z. Dang, M. Muddassir, S. Raza, A. Zhong, X. Wang and J. Jin, A New Cd(II)-Based Coordination Polymer for Efficient Photocatalytic Removal of Organic Dyes, *Molecules*, 2023, **28**(19), 6848.

27 M. Rezaei, A. A. Ensafi and E. Heydari-Bafrooei, MoS_2/$SrTiO_{3-x}$ perovskite heterostructure: Fabrication, characterization, and comprehensive photodegradation study towards Rhodamine B, *Colloids Surf., A*, 2025, **708**, 135993.

28 A. Rostami-Vartooni, A. Moradi-Saadatmand, M. Bagherzadeh and M. Mahdavi, Green synthesis of Ag/Fe_3O_4/ZrO_2 nanocomposite using aqueous Centaurea cyanus flower extract and its catalytic application for reduction of organic pollutants, *Iran. J. Catal.*, 2024, **9**(1), 27–35.

29 Y. Ao, J. Bao, P. Wang, C. Wang and J. Hou, Bismuth oxychloride modified titanium phosphate nanoplates: a new pn type heterostructured photocatalyst with high activity for the degradation of different kinds of organic pollutants, *J. Colloid Interface Sci.*, 2016, **476**, 71–78.

30 D. Zhou, B. Yu, Q. Chen, H. Shi, Y. Zhang, D. Li, X. Yang, W. Zhao, C. Liu and G. Wei, Improved visible light photocatalytic activity on Z-scheme g-C3N4 decorated TiO2 nanotube arrays by a simple impregnation method, *Mater. Res. Bull.*, 2020, **124**, 110757.

31 L. Jing, Y. Xu, C. Qin, J. Liu, S. Huang, M. He, H. Xu and H. Li, Visible-light-driven ZnFe2O4/Ag/Ag3VO4 photocatalysts with enhanced photocatalytic activity under visible light irradiation, *Mater. Res. Bull.*, 2017, **95**, 607–615.

32 A. A. Santiago, E. M. Macedo, F. K. Oliveira, R. L. Tranquilin, M. D. Teodoro, E. Longo, F. V. Motta and M. R. Bomio, Enhanced photocatalytic activity of CaMoO4/g-C3N4 composites obtained *via* sonochemistry synthesis, *Mater. Res. Bull.*, 2022, **146**, 111621.

33 M. Rezaei and A. A. Ensafi, TiO_{2-x}-MoS2 heterostructure: A study of kinetic, thermodynamic, and scavenging agents' effects in photodegradation, *Mater. Sci. Semicond. Process.*, 2025, **188**, 109162.

34 S. Li, C. Wang, K. Dong, P. Zhang, X. Chen and X. Li, MIL-101(Fe)/BiOBr S-scheme photocatalyst for promoting photocatalytic abatement of Cr(VI) and enrofloxacin antibiotic: Performance and mechanism, *Chin. J. Catal.*, 2023, **51**, 101–112.

35 C. Wang, K. Rong, Y. Liu, F. Yang and S. Li, Carbon quantum dots-modified tetra (4-carboxyphenyl) porphyrin/BiOBr S-scheme heterojunction for efficient photocatalytic antibiotic degradation, *Sci. China Mater.*, 2024, **67**, 562–572.

36 M. Liu, Y. Wan, C. Zhu, G. Chen and X. Li, FeNi bimetallic modified pg-C_3N_{4-x} and its photoelectrocatalytic hydrogen production coupling anodic oxidation, *Sep. Purif. Technol.*, 2025, **357**, 130142.

37 W. Chen, R.-Q. Yan, G.-H. Chen, M.-Y. Chen, G.-B. Huang and X.-H. Liu, Hydrothermal route to synthesize helical CdS@ZnIn2S4 core-shell heterostructures with enhanced photocatalytic hydrogeneration activity, *Ceram. Int.*, 2019, **45**, 1803–1811.

38 Z. Pan, S. Wang, R. Yan, C. Song, Y. Jin, G. Huang and J. Huang, Enhanced photocatalytic properties of Mn doped CdS catalysts by decomposition of complex precursors, *Opt. Mater.*, 2020, **109**, 110324.

39 R. Xiang, C. Zhou, Y. Liu, T. Qin, D. Li, X. Dong, M. Muddassir and A. Zhong, A new type Co(II)-based photocatalyst for the nitrofurantoin antibiotic degradation, *J. Mol. Struct.*, 2024, **1312**, 138501.

40 V. Soni, A. Khosla, P. Singh, V.-H. Nguyen, Q. V. Le, R. Selvasembian, C. M. Hussain, S. Thakur and P. Raizada, Current perspective in metal oxide based photocatalysts for virus disinfection: A review, *J. Environ. Manage.*, 2022, **308**, 114617.

41 M. Rezaei, A. A. Ensafi and E. Heydari-Bafrooei, Oxygen vacancy mediated TiO_{2-x}-MoS_2/FTO heterostructure as an efficient photoanode for photoelectrochemical water splitting, *J. Ind. Eng. Chem.*, 2025, **146**, 589–602.
42 H. Sun, Z. Tian, G. Zhou, J. Zhang and P. Li, Exploring the effects of crystal facet in Bi2WO6/BiOCl heterostructures on photocatalytic properties: a first-principles theoretical study, *Appl. Surf. Sci.*, 2019, **469**, 125–134.
43 C. You, C. Wang, M. Cai, Y. Liu, B. Zhu and S. Li, Improved Photo-Carrier Transfer by an Internal Electric Field in BiOBr/Nrich C3N5 3D/2D S-Scheme Heterojunction for Efficiently Photocatalytic Micropollutant Removal, *Acta Phys.-Chim. Sin.*, 2024, **40**, 2407014.
44 T. B. Li, G. Chen, C. Zhou, Z. Y. Shen, R. C. Jin and J. X. Sun, New photocatalyst BiOCl/BiOI composites with highly enhanced visible light photocatalytic performances, *Dalton Trans.*, 2011, **40**, 6751–6758.
45 S. Li, C. You, K. Rong, C. Zhuang, X. Chen and B. Zhang, Chemically bonded $Mn_{0.5}Cd_{0.5}S$/BiOBr S-scheme photocatalyst with rich oxygen vacancies for improved photocatalytic decontamination performance, *Adv. Powder Mater.*, 2024, **3**, 100183.
46 S. Li, K. Dong, M. Cai, X. Li and X. Chen, A plasmonic S-scheme Au/MIL-101(Fe)/BiOBr photocatalyst for efficient synchronous decontamination of Cr(VI) and norfloxacin antibiotic, *eScience*, 2024, **4**, 100208.
47 D. Kandi, A. Behera, S. Sahoo and K. Parida, CdS QDs modified BiOI/Bi_2MoO_6 nanocomposite for degradation of quinolone and tetracycline types of antibiotics towards environmental remediation, *Sep. Purif. Technol.*, 2020, **253**, 117523.
48 Y. Wang, K. Deng and L. Zhang, Visible light photocatalysis of BiOI and its photocatalytic activity enhancement by in situ ionic liquid modification, *J. Phys. Chem. C*, 2011, **115**, 14300–14308.
49 T.-H. Chen, M. Yoshida, S. Tsunekawa, J.-H. Wu, K.-Y. A. Lin and C. Hu, Development of BiOI as an effective photocatalyst for oxygen evolution reaction under simulated solar irradiation, *Catal. Sci. Technol.*, 2020, **10**, 3223–3231.
50 J. Cao, B. Xu, B. Luo, H. Lin and S. Chen, Novel BiOI/BiOBr heterojunction photocatalysts with enhanced visible light photocatalytic properties, *Catal. Commun.*, 2011, **13**, 63–68.
51 A. Mishra, N. Priyadarshini, S. Mansingh and K. Parida, Recent advancement in LaFeO3-mediated systems towards photocatalytic and photoelectrocatalytic hydrogen evolution reaction: A comprehensive review, *Adv. Colloid Interface Sci.*, 2024, **333**, 103300.
52 L. Wang, D. Yan, L. Lyu, C. Hu, N. Jiang and L. Zhang, Notable light-free catalytic activity for pollutant destruction over flower-like BiOI microspheres by a dual-reaction-center Fenton-like process, *J. Colloid Interface Sci.*, 2018, **527**, 251–259.
53 J. Luo, R. Li, Y. Chen, X. Zhou, X. Ning, L. Zhan, L. Ma, X. Xu, L. Xu and L. Zhang, Rational design of Z-scheme LaFeO3/SnS2 hybrid with boosted visible light photocatalytic activity towards tetracycline degradation, *Sep. Purif. Technol.*, 2019, **210**, 417–430.
54 H. Aghaei and M. Ghiaci, Use of H_3PO_4/ZrO_2–TiO_2–surfactant mixed oxide for catalytic vapor-phase dehydration of 1-octanol, Reaction Kinetics, *Mech. Catal.*, 2020, **131**, 233–246.
55 X. Xiao and W.-D. Zhang, Facile synthesis of nanostructured BiOI microspheres with high visible light-induced photocatalytic activity, *J. Mater. Chem.*, 2010, **20**, 5866–5870.
56 J. Qin, L. Lin and X. Wang, A perovskite oxide LaCoO 3 cocatalyst for efficient photocatalytic reduction of CO 2 with visible light, *Chem. Commun.*, 2018, **54**, 2272–2275.
57 J. Guo, Y.-z Dai, X.-j Chen, L.-l Zhou and T.-h Liu, Synthesis and characterization of Ag3PO4/LaCoO3 nanocomposite with superior mineralization potential for bisphenol A degradation under visible light, *J. Alloys Compd.*, 2017, **696**, 226–233.
58 D. Kumar, G. Agarwal, B. Tripathi, D. Vyas and V. Kulshrestha, Characterization of PbS nanoparticles synthesized by chemical bath deposition, *J. Alloys Compd.*, 2009, **484**, 463–466.
59 A. K. Zak, W. A. Majid, M. E. Abrishami and R. Yousefi, X-ray analysis of ZnO nanoparticles by Williamson–Hall and size–strain plot methods, *Solid State Sciences*, 2011, **13**, 251–256.
60 N. Pourshirband, A. Nezamzadeh-Ejhieh and S. N. Mirsattari, The CdS/g-C3N4 nano-photocatalyst: brief characterization and kinetic study of photodegradation and mineralization of methyl orange, *Spectrochim. Acta, Part A*, 2021, **248**, 119110.
61 M. Sakthivel, S. Ramaraj, S.-M. Chen and B. Dinesh, Synthesis of rose like structured LaCoO3 assisted functionalized carbon nanofiber nanocomposite for efficient electrochemical detection of anti-inflammatory drug 4-aminoantipyrine, *Electrochimica Acta*, 2018, **260**, 571–581.
62 S. Qu, Y. Xiong and J. Zhang, Fabrication of GO/CDots/BiOI nanocomposites with enhanced photocatalytic 4-chlorophenol degradation and mechanism insight, *Sep. Purif. Technol.*, 2019, **210**, 382–389.
63 Z. Jiang, W. Wan, H. Li, S. Yuan, H. Zhao and P. K. Wong, A hierarchical Z-scheme α-Fe2O3/g-C3N4 hybrid for enhanced photocatalytic CO2 reduction, *Adv. Mater.*, 2018, **30**, 1706108.
64 C. Li, A. Zhang, L. Zhang, J. Song, S. Su, Z. Sun and J. Xiang, Enhanced photocatalytic activity and characterization of magnetic Ag/BiOI/ZnFe2O4 composites for Hg0 removal under fluorescent light irradiation, *Appl. Surf. Sci.*, 2018, **433**, 914–926.
65 L. Yosefi and M. Haghighi, Fabrication of nanostructured flowerlike p-BiOI/p-NiO heterostructure and its efficient photocatalytic performance in water treatment under visible-light irradiation, *Appl. Catal., B*, 2018, **220**, 367–378.
66 A. Sobhani-Nasab, M. Eghbali-Arani, S. M. Hosseinpour-Mashkani, F. Ahmadi and M. Rahimi-Nasrabadi, Eco-friendly preparation and characterization of CuMn2O4 nanoparticles with the green capping agent and their

photocatalytic and photovoltaic applications, *Iran. J. Catal.*, 2024, **10**(2), 91–99.

67 H. R. Pouretedal, M. Fallahgar, F. Sotoudeh Pourhasan and M. Nasiri, Taguchi optimization of photodegradation of yellow water of trinitrotoluene production catalyzed by nanoparticles TiO2/N under visible light, *Iran. J. Catal.*, 2024, **7**(4), 317–326.

68 N. Omrani and A. Nezamzadeh-Ejhieh, A quadripartite Cu2O-CdS-BiVO4-WO3 visible-light driven photocatalyst contained three cascade Z-scheme systems: Focus on conditions' optimization, scavenging agents and the mechanism pathway towards sulfasalazine, *Iran. J. Catal.*, 2025, DOI: 10.57647/j.ijc.2025.1502.15.

69 N. Mehrabanpour, A. Nezamzadeh-Ejhieh, S. Ghattavi and A. Ershadi, A magnetically separable clinoptilolite supported CdS-PbS photocatalyst: Characterization and photocatalytic activity toward cefotaxime, *Appl. Surf. Sci.*, 2023, **614**, 156252.

70 S. K. Suram, P. F. Newhouse and J. M. Gregoire, High Throughput Light Absorber Discovery, Part 1: An Algorithm for Automated Tauc Analysis, *ACS Comb. Sci.*, 2016, **18**, 673–681.

71 P. Norouzzadeh, K. Mabhouti, M. Golzan and R. Naderali, Investigation of structural, morphological and optical characteristics of Mn substituted Al-doped ZnO NPs: a Urbach energy and Kramers-Kronig study, *Optik*, 2020, **204**, 164227.

72 P. Makuła, M. Pacia and W. Macyk, How To Correctly Determine the Band Gap Energy of Modified Semiconductor Photocatalysts Based on UV–Vis Spectra, *J. Phys. Chem. Lett.*, 2018, **9**, 6814–6817.

73 J. Tauc, *Optical Properties of Solids*, ed. F. Abeles, North-Holland Publishing Company, Amsterdam, 1972, ch. 5.

74 J. B. Coulter and D. P. Birnie III, Assessing Tauc Plot Slope Quantification: ZnO Thin Films as a Model System, *Phys. Status Solidi B*, 2018, **255**, 1700393.

75 R. Köferstein, L. Jäger and S. G. Ebbinghaus, Magnetic and optical investigations on LaFeO3 powders with different particle sizes and corresponding ceramics, *Solid State Ionics*, 2013, **249–250**, 1–5.

76 R. Köferstein and S. G. Ebbinghaus, Investigations of $BaFe_{0.5}Nb_{0.5}O_3$ nano powders prepared by a low temperature aqueous synthesis and resulting ceramics, *J. Eur. Ceram. Soc.*, 2017, **37**, 1509–1516.

77 K.-i Katsumata, R. Motoyoshi, N. Matsushita and K. Okada, Preparation of graphitic carbon nitride (g-C3N4)/WO3 composites and enhanced visible-light-driven photodegradation of acetaldehyde gas, *J. Hazard. Mater.*, 2013, **260**, 475–482.

78 P. Kubelka, Ein beitrag zur optik der farbanstriche, *Z. tech. Phys*, 1931, **12**, 593–601.

79 J. Tauc, R. Grigorovici and A. Vancu, Optical properties and electronic structure of amorphous germanium, *Phys. Status Solidi B*, 1966, **15**, 627–637.

80 S. Shanthi, S. Poovaragan, M. Arularasu, S. Nithya, R. Sundaram, C. M. Magdalane, K. Kaviyarasu and M. Maaza, Optical, magnetic and photocatalytic activity studies of Li, Mg and Sr doped and undoped zinc oxide nanoparticles, *J. Nanosci. Nanotechnol.*, 2018, **18**, 5441–5447.

81 B. Manikandan and R. John, Properties of sol-gel synthesized multiphase TiO2 (AB)-ZnO (ZW) semiconductor nanostructure: An effective catalyst for methylene blue dye degradation, *Iran. J. Catal.*, 2024, **10**(1), 1–16.

82 Y. Nosaka and A. Y. Nosaka, Generation and detection of reactive oxygen species in photocatalysis, *Chem. Rev.*, 2017, **117**, 11302–11336.

83 S. Dianat, Visible light induced photocatalytic degradation of direct red 23 and direct brown 166 by InVO4-TiO2 nanocomposite, *Iran. J. Catal.*, 2024, **8**(2), 121–132.

84 A. Eslami, A. Oghazyan and M. Sarafraz, Magnetically separable $MgFe_2O_4$ nanoparticle for efficient catalytic ozonation of organic pollutants, *Iran. J. Catal.*, 2024, **8**(2), 95–102.

85 N. Elmi Fard and R. Fazaeli, Experimental design study of RB 255 photocatalytic degradation under visible light using synthetic Ag/TiO2 nanoparticles: Optimization of experimental conditions, *Iran. J. Catal.*, 2024, **8**(2), 133–141.

86 N. Parsafard, Optimization of main parameters affecting activity and octane number produced from catalytic isomerization of n-heptane using response surface methodology, *Iran. J. Catal.*, 2023, **13**, 125–133.

87 S. A. Hosseini and R. Saeedi, Photocatalytic degradation of rhodamine B by nano bismuth oxide: Process modeling by response surface methodology (RSM), (2017).

88 A. Nezamzadeh-Ejhieh and H. Zabihi-Mobarakeh, Heterogeneous photodecolorization of mixture of methylene blue and bromophenol blue using CuO-nano-clinoptilolite, *J. Ind. Eng. Chem.*, 2014, **20**, 1421–1431.

89 A. Yousefi and A. Nezamzadeh-Ejhieh, Preparation and characterization of SnO2-BiVO4-CuO catalyst and kinetics of phenazopyridine photodegradation, *Iran. J. Catal.*, 2021, **11**, 247–259.

90 R. J. Manikandan Balakrishnan, Properties of sol-gel synthesized multiphase TiO2 (AB)-ZnO (ZW) semiconductor nanostructure: an effective catalyst for methylene blue dye degradation, *Iran. J. Catal.*, 2020, **10**, 1–16.

91 R. Sheikhsamany, A. Nezamzadeh-Ejhieh, R. Ensandoost and B. Kakavandi, BaTi0. 85Zr0. 15O3/MOF-5 nanocomposite: Synthesis, characterization and photocatalytic activity toward tetracycline, *J. Mol. Liq.*, 2024, **403**, 124850.

92 R. Sheikhsamany, H. Faghihian and M. Shirani, The MIL100 (Fe)/$BaTi_{0.85}Zr_{0.15}O_3$ nanocomposite with the photocatalytic capability for study of tetracycline photodegradation kinetics, *Spectrochim. Acta, Part A*, 2023, **291**, 122323.

93 B. Divband, A. Jodaie and M. Khatmian, Enhancement of photocatalytic degradation of 4-nitrophenol by integrating Ag nanoparticles with ZnO/HZSM-5 nanocomposite, *Iran. J. Catal.*, 2024, **9**(1), 63–70.

94 S. D. Khairnar, M. R. Patil and V. S. Shrivastava, Hydrothermally synthesized nanocrystalline Nb2O5 and its visible-light photocatalytic activity for the degradation of

congo red and methylene blue, *Iran. J. Catal.*, 2024, **8**(2), 143–150.

95 M. Zebardast, A. Fallah Shojaei and K. Tabatabaeian, Enhanced removal of methylene blue dye by bimetallic nano-sized MOF-5s, *Iran. J. Catal.*, 2024, **8**(4), 297–309.

96 K. Govindan, H. T. Chandran, M. Raja, S. U. Maheswari and M. Rangarajan, Electron scavenger-assisted photocatalytic degradation of amido black 10B dye with Mn3O4 nanotubes: a response surface methodology study with central composite design, *J. Photochem. Photobiol., A*, 2017, **341**, 146–156.

97 D. Vione, S. Khanra, S. C. Man, P. R. Maddigapu, R. Das, C. Arsene, R.-I. Olariu, V. Maurino and C. Minero, Inhibition *vs*. enhancement of the nitrate-induced phototransformation of organic substrates by the OH scavengers bicarbonate and carbonate, *Water Res.*, 2009, **43**, 4718–4728.

98 T. Tan, D. Beydoun and R. Amal, Effects of organic hole scavengers on the photocatalytic reduction of selenium anions, *J. Photochem. Photobiol., A*, 2003, **159**, 273–280.

99 A. Nandi and I. Chatterjee, Scavenging of superoxide radical by ascorbic acid, *J. Biosci.*, 1987, **11**, 435–441.

100 S. Sultana, S. Mansingh and K. M. Parida, Facile Synthesis of CeO_2 Nanosheets Decorated upon BiOI Microplate: A Surface Oxygen Vacancy Promoted Z-Scheme-Based 2D-2D Nanocomposite Photocatalyst with Enhanced Photocatalytic Activity, *J. Phys. Chem. C*, 2018, **122**, 808–819.

101 J. Zhang, G. Yu, C. Yang and S. Li, Recent progress on S-scheme heterojunction strategy enabling polymer carbon nitrides C3N4 and C3N5 enhanced photocatalysis in energy conversion and environmental remediation, *Curr. Opin. Chem. Eng.*, 2024, **45**, 101040.

102 S. Li, K. Rong, X. Wang, C. Shen, F. Yang and Q. Zhang, Design of Carbon Quantum Dots/CdS/Ta3N5 S-Scheme Heterojunction Nanofibers for Efficient Photocatalytic Antibiotic Removal, *Acta Physico-Chimica Sinica*, 2024, **40**, 2403005.

103 Z.-C. Zhao, K. Wang, L. Chang, R.-Q. Yan, J. Zhang, M. Zhang, L. Wang, W. Chen and G.-B. Huang, Construction of S-scheme MIL-101(Fe)/Bi2MoO6 heterostructures for enhanced catalytic activities towards tetracycline hydrochloride photodegradation and nitrogen photofixation, *Solar Energy*, 2023, **264**, 112042.

104 H. Yang, Z.-C. Zhao, Y.-P. Yang, Z. Zhang, W. Chen, R.-Q. Yan, Y. Jin and J. Zhang, Defective WO3 nanoplates controllably decorated with MIL-101(Fe) nanoparticles to efficiently remove tetracycline hydrochloride by S-scheme mechanism, *Sep. Purif. Technol.*, 2022, **300**, 121846.

105 Q. Xu, L. Zhang, J. Yu, S. Wageh, A. A. Al-Ghamdi and M. Jaroniec, Direct Z-scheme photocatalysts: Principles, synthesis, and applications, *Mater. Today*, 2018, **21**, 1042–1063.

106 P. Priyadarshini, A. Mishra, A. Majhi, K. Parida and K. Parida, Engineering rGO–Driven Z-Scheme Charge Dynamics in NH2-MIL-125(Ti)/ZIF-67 for Superior Green Energy Applications, *ACS Appl. Energy Mater.*, 2025, **8**(8), 5067–5081.

107 K. Sharma, V. Hasija, M. Malhotra, P. K. Verma, A. A. Parwaz Khan, S. Thakur, Q. Van Le, H. H. Phan Quang, V.-H. Nguyen, P. Singh and P. Raizada, A review of CdS-based S-scheme for photocatalytic water splitting: Synthetic strategy and identification techniques, *Int. J. Hydrogen Energy*, 2024, **52**, 804–818.

108 Y. Kumar, A. Sudhaik, K. Sharma, Sonu, P. Raizada, A. Aslam Parwaz Khan, V.-H. Nguyen, T. Ahamad, P. Singh and A. M. Asiri, Construction of magnetically separable novel arrow down dual S-scheme ZnIn2S4/BiOCl/FeVO4 heterojunction for improved photocatalytic activity, *J. Photochem. Photobiol., A*, 2023, **435**, 114326.

109 M. Malhotra, K. Poonia, P. Singh, A. A. P. Khan, P. Thakur, Q. Van Le, E. T. Helmy, T. Ahamad, V.-H. Nguyen, S. Thakur and P. Raizada, An overview of improving photocatalytic activity of MnO2 *via* the Z-scheme approach for environmental and energy applications, *J. Taiwan Inst. Chem. Eng.*, 2024, **158**, 104945.

110 A. Kumar, P. Singh, V.-H. Nguyen, Q. Van Le, T. Ahamad, S. Thakur, L. Huong Nguyen and P. Raizada, Rationally constructed synergy between dual-vacancies and Z-scheme heterostructured MoS2-x/g-C3N4/Ca-α-Fe2O3 for high-performance photodegradation of sulfamethoxazole antibiotic from aqueous solution, *Chem. Eng. J.*, 2023, **474**, 145720.

111 K. Sharma, A. Sudhaik, P. Raizada, P. Thakur, X. M. Pham, Q. Van Le, V.-H. Nguyen, T. Ahamad, S. Thakur and P. Singh, Constructing α-Fe2O3/g-C3N4/SiO2 S-scheme-based heterostructure for photo-Fenton like degradation of rhodamine B dye in aqueous solution, *Environ. Sci. Pollut. Res.*, 2023, **30**, 124902.

112 V. Dutta, S. Sonu, P. Raizada, V. K. Thakur, T. Ahamad, S. Thakur, P. Kumar Verma, H. H. P. Quang, V.-H. Nguyen and P. Singh, Prism-like integrated Bi2WO6 with Ag-CuBi2O4 on carbon nanotubes (CNTs) as an efficient and robust S-scheme interfacial charge transfer photocatalyst for the removal of organic pollutants from wastewater, *Environ. Sci. Pollut. Res.*, 2023, **30**, 124530.

113 M. Sheydaei, H. R. K. Shiadeh, B. Ayoubi-Feiz and R. Ezzati, Preparation of nano N-TiO2/graphene oxide/titan grid sheets for visible light assisted photocatalytic ozonation of cefixime, *Chem. Eng. J.*, 2018, **353**, 138–146.

114 M. Sheydaei, P. Moharramkhani, B. Ayoubi-Feiz and F. Khodabandeloo, Experimental and computational investigation of cold atmospheric plasma/visible-light/N-TiO2 in treatment of synthetic and real wastewaters, *Water Resour. Ind.*, 2025, **33**, 100276.

115 S. O. Babalola, P. A. Steenkamp, M. O. Daramola and S. A. Iwarere, Mechanistic study of cefixime degradation with an atmospheric air dielectric barrier discharge – Influence of radical scavengers and metal ion catalyst, *Sep. Purif. Technol.*, 2025, **353**, 128376.

116 F. Mahdavian, A. Dargahi, M. Vosoughi, A. Mokhtari, H. Sadeghi and Y. Rashtbari, Enhanced removal of cefixime from aqueous solutions using Fe3O4@GO nanocomposite with ultrasonic: isotherm and kinetics study, *Desalin. Water Treat.*, 2022, **280**, 224–239.

117 S. Aber, L. Ghalamchi, H. Hosseinzadeh, K. Nofouzi and A. Naseri, Biological treatment of ranitidine and cefixime trihydrate mixed solution by activated sludge in sequencing batch reactor, *Desalin. Water Treat.*, 2021, **225**, 94–103.